CHAPTER 99

3-D Analysis of Flow around a Vertical Cylinder on a Scoured Bed

Tomonao Kobayashi[1]

ABSTRACT

Velocity distributions around a vertical cylinder on a scoured seabed under waves have been evaluated in three dimensions using a laser Doppler anemometer and the mass-consisstent model to explain the mechanism of local scouring in the wave fields. Through their comparisons with the measurements over a flat bottom under the same conditions, effects of the scoured seabed configuration on the vortex behavior around a cylinder and the near-bed flow structures have been clarified. Namely, the scoured seabed topography causes deformation of the vortices and the flow field from a quasi-two-dimensional structure observed above the flat bed into a complex three-dimensional structure. The flow around a cylinder has also been simulated numerically with a three-dimensional vortex segment model. The results have shown a good agreement with those in the experiments.

1. INTRODUCTION

Prediction of local scouring around nearshore and offshore structures is a need for engineers, and many researchers have been challenging to estimate the scour depth and shape. For example, Well and Sorensen (1970) have found the relationships of the ultimate scour depth with the Shields number, Reynolds number, etc. in experiments. Sumer *et al.* (1992) have reported laboratory tests on the scouring and expressed the scour depth as a function of the Keulegan-Carpenter (K.C.) number with continuous sediment motion on beds. However, to develop a reliable prediction model for the local scouring, we need a deeper understanding of the scouring mechanism and the flow features near the bed around structures.

Characteristics of the flow around a vertical cylinder in steady currents have been investigated extensively (*e.g.*, Shen *et al.*, 1969; Breusers *et al.*, 1977). It has been found that a horseshoe vortex above the scoured bed is a dominant factor in the scour process, and that the vortex has a close relationship with the bed profile near the cylinder. The vortex behavior above the scoured bed is thus a very important factor to consider in the estimation of scouring.

[1]Research Associate, Department of Civil Engineering, Tokyo Rika University, 2641 Yamazaki, Noda city, Chiba, 278 Japan.

Table 1. Conditions of laboratory experiments.

Water Depth	h	100 mm
Water Period	T	1.5 s
Wave Height	H	38 mm
Ursell Number	U_r	83.8
Cylinder Diameter	D	48 mm
Maximum Velocity above the Bed	$U_{\max}$	167 mm/s
Keulegan-Carpenter Number	K.C.	5.2

In the wave-related field, relatively few studies have been conducted on this topic. Nishizawa and Sawamoto (1988) and Sumer *et al.* (1992) have studied the flow around a vertical slender cylinder under waves using flow visualization techniques. They have reported relationships between the flow characteristics and the K.C. number based on experimental results for a flat bottom only. In case of a scoured bed, there has been even less literature, probably because the flow near the scoured seabed shows a highly complex three-dimensional pattern owing to the complicated scour shape and the unsteadiness of the main flow itself. It should be emphasized, however, this unsteady three-dimensional near-bed flow with vortices governs the local scouring around the cylinder.

The purpose of this study is to recognize the characteristics of the flow around a vertical cylinder on the scoured bed under waves. First, to show the typical features of the flow and vortices, the measurements of three-dimensional velocity distributions around the cylinder are presented for cases of both the flat bottom and the scoured bed, Then, the results of flow simulation are shown, which have been obtained with a numerical model developed as an initial step to build up a local scouring model.

2. EXPERIMENTAL PROCEDURE

2. 1. Experimental Conditions

Velocity distributions have been measured around a vertical slender cylinder on the flat bottom and on the scoured seabed under the same conditions, which are shown in *Table 1.* The reason why these conditions have been selected is that under them, clear scouring had occurred on a movable bed as described below. *Figure 1* shows the time variation of a water surface elevation in one wave period and the vertical distributions of horizontal velocity near the flat bottom at several phases without disturbances due to the cylinder.

In order to determine the scoured bottom topography around the cylinder, a movable bed test has been conducted using sand with the medium diameter $d_{50} = 0.6$mm and the density $\rho_s = 2.68$g/cm^3, for which the maximum Shields number Ψ_m is 0.025.

The modified final topography is shown in *Fig. 2*, where the wave direction is form the left to the right. The coordinates x, y and z are in the streamwise, the lateral and the vertical directions, respectively, and their origin is set on the centerline of the cylinder at the elevation the initial flat bottom. The actual

scoured bed topography has been almost symmetric with respect to the vertical x-z plane. Furthermore, as explained later, the flow pattern has been also satisfactorily symmetric. Hence the bed profile has been modified to be symmetric and employed in the following experiment.

As shown in *Fig. 2*, a pair of deep scour holes are found at the two side edges of the cylinder (the hatched part), and two hills are formed near the downwave edges.

2. 2. Experimental Apparatus

Velocity distributions around the vertical cylinder were measured in full detail using a two-dimensional laser Doppler anemometer, which was set on a movable

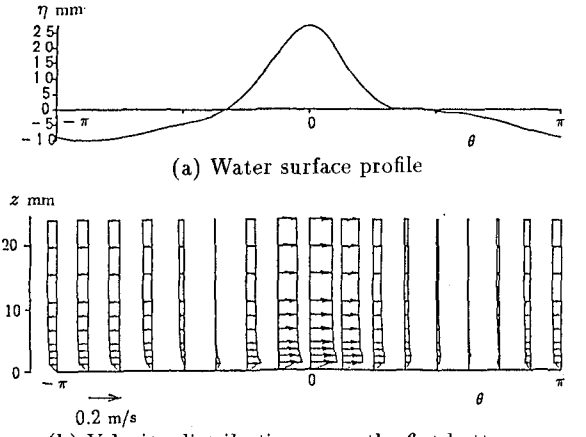

(a) Water surface profile

(b) Velocity distributions near the flat bottom

Fig. 1. Water surface profile and velocity distributions above the flat bottom.

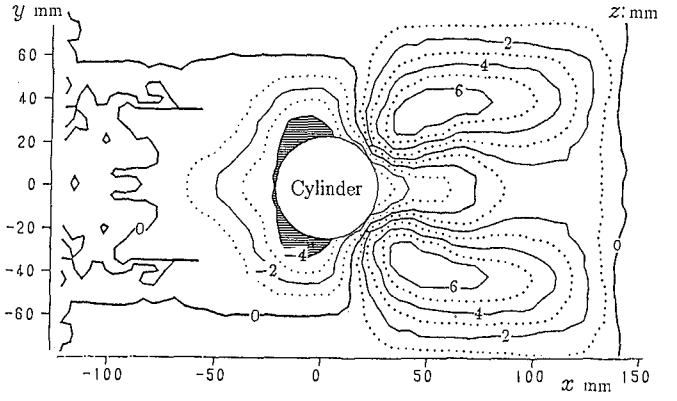

Fig. 2. Contour map of the scoured bed around a vertical cylinder.

table. A personal computer was used to control the movable table and a wave maker, and to acquire the output from the anemometer and a wave gage. Thus the velocity distributions around the cylinder near the bottom were automatically recorded by the computer. Nearly 5,000 points of velocity measurement were distributed around the cylinder, and the phase-average velocity data for 100 waves were obtained at each point.

Since the K.C. number is low as shown in *Table 1*, the flow pattern was highly symmetric with respect to the vertical x-z plane; the symmetry plane is $y = 0$mm. Therefore the velocity distributions were measured only in one side ($y \geq 0$). The anemometer directly measured only the two velocity components u and w, in the x and z directions, respectively. The velocity component v in the y direction was not measured but estimated with the following MASCON model.

2. 3. MASCON Model

The MASCON (mass-consistent) model, developed by Sherman (1978) to adjust field measurement data of wind, is useful to estimate three-dimensional velocity distributions as properly adjusted in a mass-consistent flow field over a complex topography. This model has often been applied to the adjustment of the field velocity data in meteorology. However, its applications to laboratory experiments are very few (*e.g.*, Hino *et al.*, 1989). In the present study, this model is applied to the evaluation of the velocity component v, which was not measured in the experiments.

The specific function of this model is

$$E(u, v, w, \lambda) = \int_V \left[\alpha_x{}^2(u - u_0)^2 + \alpha_y{}^2(v - v_0)^2 + \alpha_z{}^2(w - w_0)^2 + \lambda\left(\frac{\partial u}{\partial x} + \frac{\partial v}{\partial y} + \frac{\partial w}{\partial z}\right)\right] dx\, dy\, dz \tag{1}$$

where u_0, v_0 and w_0 are observed velocity components, u, v and w are adjusted ones, λ is the Lagrange multiplier, and each α is a Gauss precision modulus.

The solutions which minimize a value of this function E satisfy the following relations.

$$u = u_0 + \frac{1}{2\alpha_x{}^2}\frac{\partial \lambda}{\partial x} \tag{2}$$

$$v = v_0 + \frac{1}{2\alpha_y{}^2}\frac{\partial \lambda}{\partial y} \tag{3}$$

$$w = w_0 + \frac{1}{2\alpha_z{}^2}\frac{\partial \lambda}{\partial z} \tag{4}$$

$$\frac{\partial u}{\partial x} + \frac{\partial v}{\partial y} + \frac{\partial w}{\partial z} = 0 \tag{5}$$

$$\frac{1}{\alpha_x{}^2}\frac{\partial^2 \lambda}{\partial x^2} + \frac{1}{\alpha_y{}^2}\frac{\partial^2 \lambda}{\partial y^2} + \frac{1}{\alpha_z{}^2}\frac{\partial^2 \lambda}{\partial z^2} = -2\left(\frac{\partial u_0}{\partial x} + \frac{\partial v_0}{\partial y} + \frac{\partial w_0}{\partial z}\right) \tag{6}$$

Values of the adjusted velocity component u, v and w are estimated from *Eqs.* (2) to (6).

Since the purpose of the application of this model to the present study is to evaluate the velocity component v from the other two measured velocity components u_0 and w_0, the condition that ${\alpha_y}^2$ is larger enough than ${\alpha_x}^2$ and ${\alpha_z}^2$ must be introduced. Otherwise the adjusted velocity components u and w would severely deviate from the measurements of u_0 and w_0 in this model. Hence, values 1.0, 5.0 and 1.0 are employed for α_x, α_y and α_z, respectively, and v_0 is set to be zero in this study.

3. EXPERIMENTAL RESULTS

3. 1. Flow Field above the Flat Bottom

First the velocity distributions above the flat bottom were measured under the conditions given in *Table 1*. *Figure 3* shows the phase-average velocity distributions in horizontal planes at z = 2mm and z = 8mm. The direction of wave propagation is from the left to the right, and the phase $\theta = 0$ corresponds to the time when the wave crest passes the location of the cylinder. Since *Fig. 3* shows the velocity distributions in horizontal planes, the velocity components u and v are indicated by vectors, and the w-component is shown as contour lines in the figure. Solid and dashed contour lines mean ascending and descending flows, respectively.

A pair of vortices are shed in the wake region after the passing of the wave crest or the trough as shown in *Fig. 3* b, d, g and i. As the waves are finite amplitude waves, whose Ursell number is 83.8, the main flow under the wave crest is much stronger than that under the wave trough as shown in *Figs. 1* and *3*. However, the weak opposite-directional main flow continues longer than the strong shoreward flow under the wave crest. Hence, the vortices shedding from the cylinder at the up-wave side of the cylinder grow bigger than the ones at the down-wave side of the cylinder as represented in *Fig. 3* b, d, g and i. These vortices at the up-wave side of the cylinder induce the intense flow on the surface of the cylinder, as shown in *Fig. 3* e and j. Then, this intense flow supposedly picks up sand and forms a pair of the scour holes at the two side edge of the cylinder in *Fig. 2*. According to the contour maps showing the distributions of w, concentration of the intense descending flow occurs in the wake, whereas the weak ascending flow regions extend widely around the cylinder to balance the descending flow.

The difference of the velocity distributions between the planes at z = 2mm and z = 8mm is negligible. The velocity distribution at the plane z = 22mm is also similar to them. This indicates that the flow field above the flat bottom is approximately two-dimensional, namely, uniform in the vertical direction.

Figure 4 shows the distributions of the flow with vorticity vectors at the wave phase $\theta = \pi/8$, immediately after the wave crest passing. It is seen in *Fig. 4*, the axis of the vortex shed from the cylinder is nearly vertical. This fact also means that the flow field above the flat bottom is almost two-dimensional or uniform in the vertical direction. The shed vortex is deformed down-wave near the bottom owing to the strong descending flow in the wake.

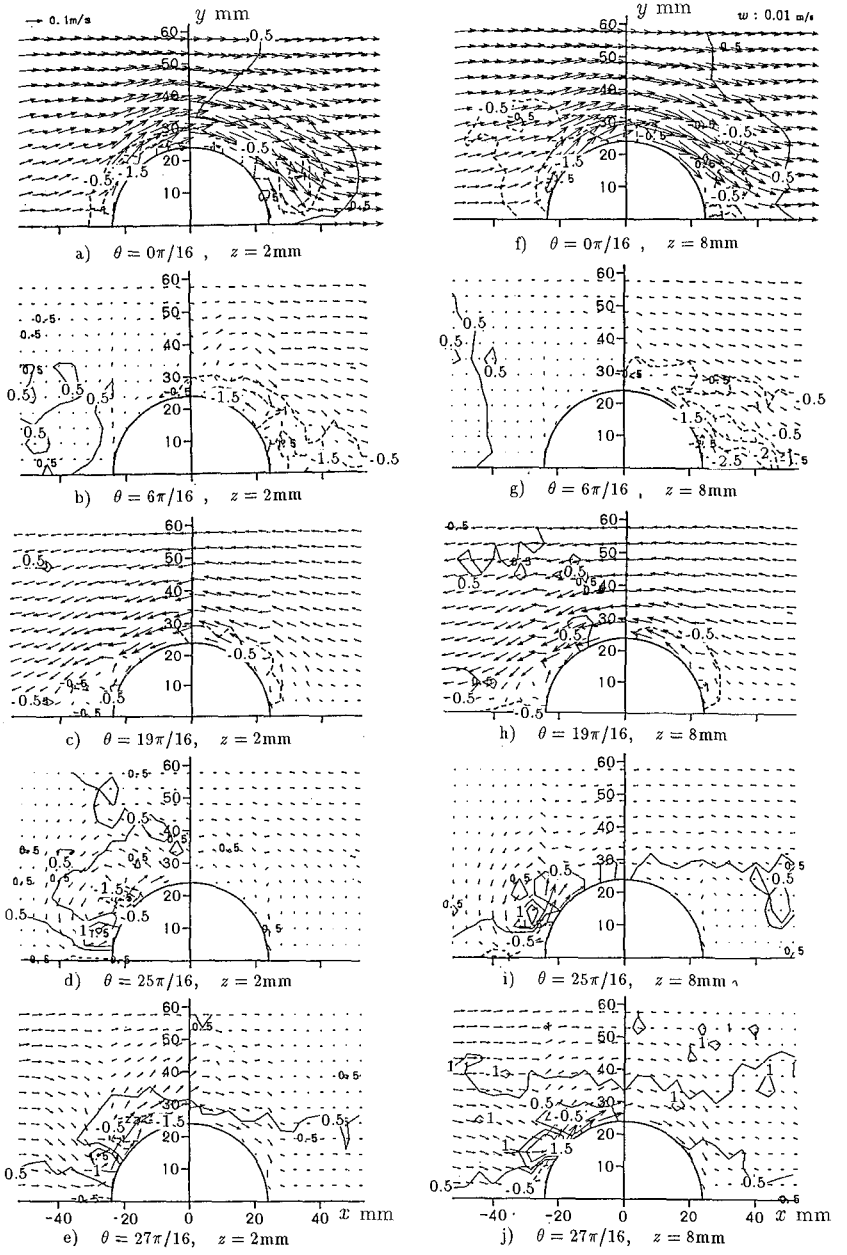

Fig. 3. Phase-average velocity distributions in horizontal planes at $z = 2$mm and $z = 8$mm above the flat bottom. Solid and dashed contour lines show ascending and descending flows (w-component) respectively.

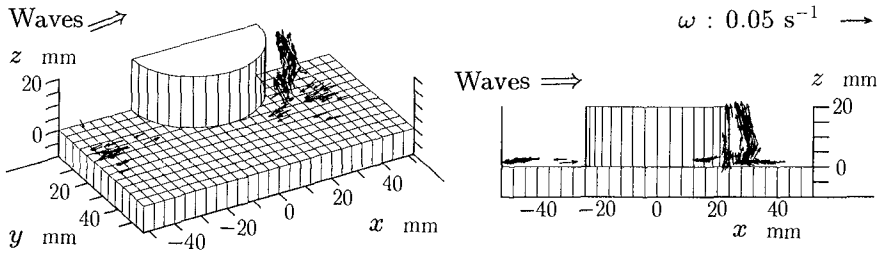

(a) $\theta = \pi/8$ (Bird's-eye view) (b) $\theta = \pi/8$ (Side view)

Fig. 4. Vorticity vector distributions above the flat bottom at $\theta = \pi/8$.

3. 2. Flow Field above the Scoured Seabed

The velocity distributions above the scoured seabed were measured under the same conditions with those for the flat bottom (*Table 1*). To perform the measurement, the scoured bottom topography shown in *Fig. 2* was modeled in wood and surfaced with sand of $d_{50} = 0.6$mm. *Figure 5* shows the velocity distributions in horizontal planes at different heights above the scoured seabed at $\theta = 0$ and $\theta = \pi/4$. The flow structure is very complex because of the scoured bed topography. It is observed that the flow rises over the slope from the scour hole to the hill, and that strong ascending flow occurs at the down-wave side edge of the cylinder. At the phase $\theta = \pi/4$, the wake grows in the lee of the cylinder, where the strong flow toward the opposite direction appears at the heights $z = 6$mm and $z = 10$mm. This is not clearly observed at other heights.

Figure 6 shows the velocity distributions in the vertical x-z planes at the phase $\theta = \pi/4$, in which the cylinder is represented by pairs of the vertical straight lines, the velocity components u and w are shown as vectors, and the v-component is indicated by contour lines. The direction of wave propagation is again from the left to the right. In the symmetry plane ($y = 0$mm), the descending flow appears in the wake, while in the other planes a vortex with a horizontal axis is clearly seen.

Figure 7 shows the time evolution of this horizontal vortex. The vortex develops as the wake grows after the wave crest passing, and then it disappears when the main flow decelerates. It is observed from this figure that this vortex induces local intense flow near the bed in a very short period. Under the present conditions, the intensity of this flow was enough to pick up sand. Then, it is seemed that this vortex has a close relationship with the local scouring around the cylinder.

The structure and the time evolution of the vortex are shown in *Figs. 8* and *9*, respectively, with vorticity vectors. The bird's-eye view in *Fig. 8* shows that an arch-shaped vortex with its feet on the hills is formed in the lee of the cylinder, and the side view indicates that the vortex leans down-wave. The vortex concentration is strong at the feet and becomes weak upward or towards the symmetry plane.

According to *Fig. 9*, the arch-shaped vortex does not appear immediately

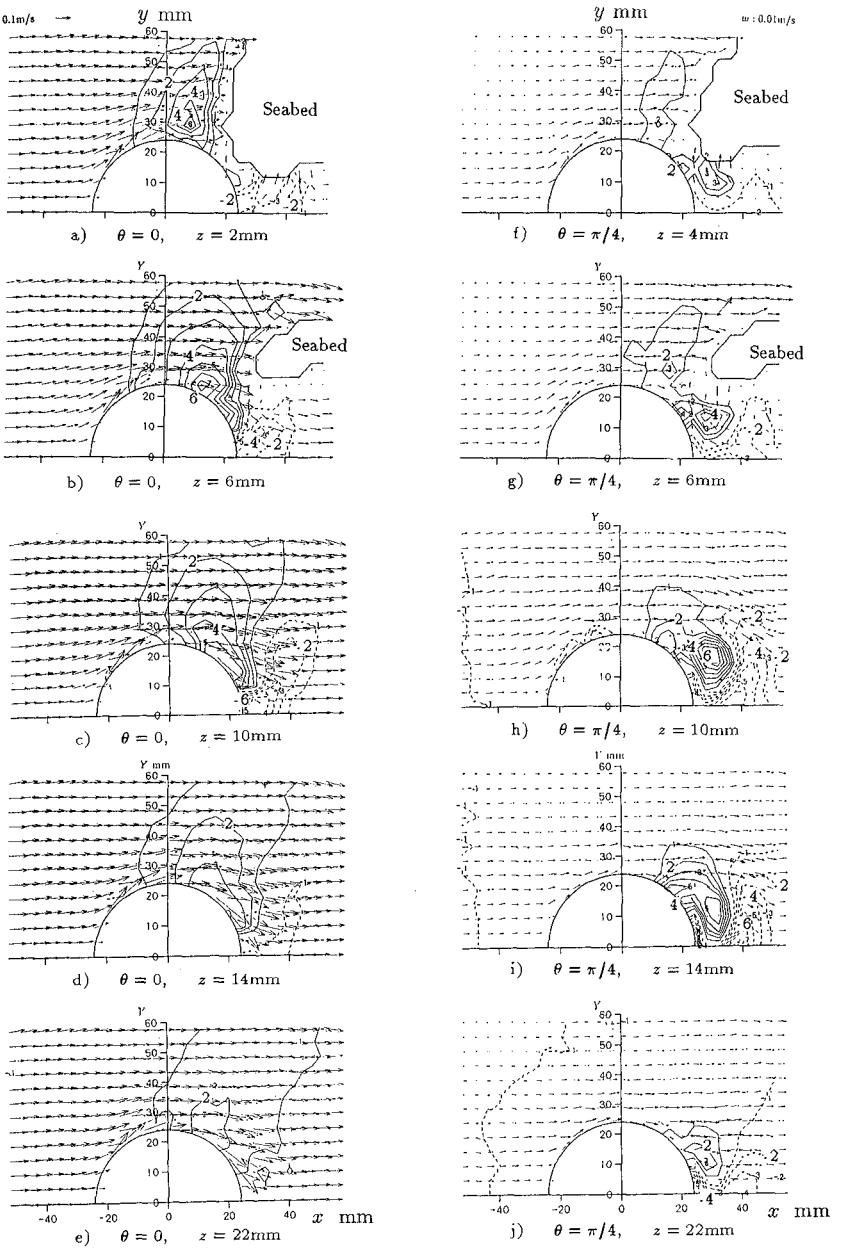

Fig. 5. Velocity distributions in horizontal planes above the scoured seabed.

before and at the phase of wave crest passing ($\theta = 0$); the vortex starts to be produced soon after the crest passing, and then gradually develops and leans down-wave. It is concluded from *Fig. 9* that the interaction of the vortex shed from the cylinder and the separation over the hills induces the arch-shaped vortex above the scoured bed.

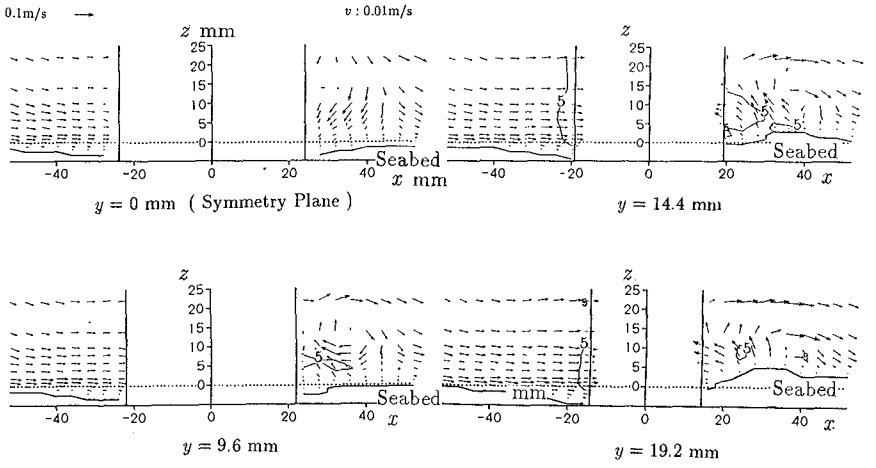

Fig. 6. Velocity distributions in vertical planes above the scoured seabed at $\theta = \pi/4$.

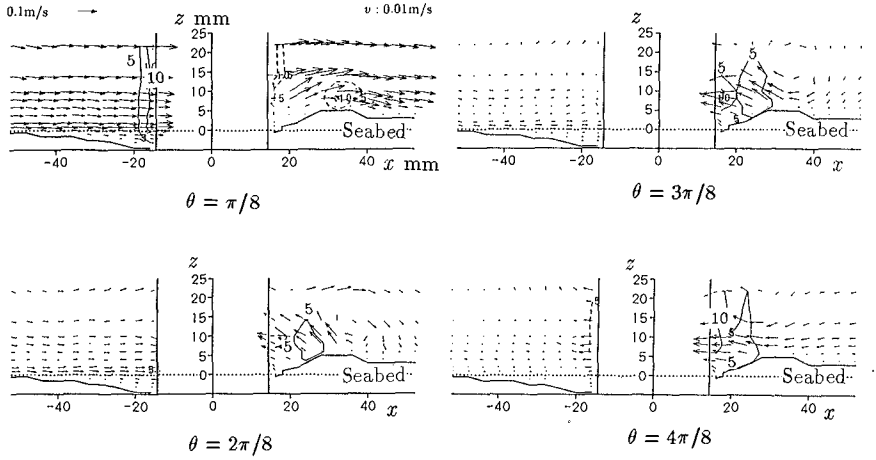

Fig. 7. Time evolution of the horizontal vortex ($y = 19.2$mm).

3. 3. Comparison between the Two Flow Fields

The results of the two experiments are compared to study the effects of the bottom profile on the flow structures.

The vorticity vector distributions in *Fig. 4* indicate that the axis of the vortex shed from the cylinder is almost vertical above the flat bottom. Consequently the flow structure does not change significantly in the vertical direction. On the other hand, as shown in *Figs. 8* and *9*, the velocity distributions over the scoured seabed are very complex and the vortex is deformed into arch-shape. The separation over the hill forces the vortex shed from the cylinder to change to this

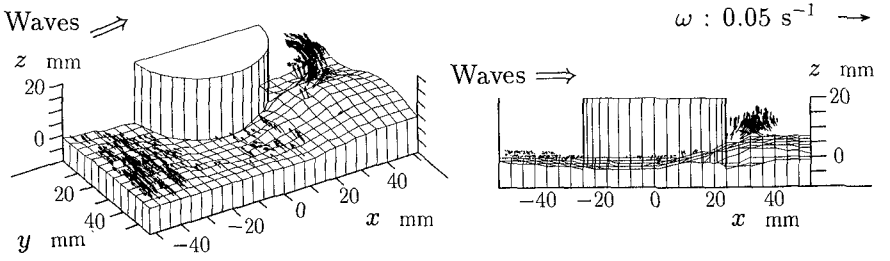

(a) $\theta = \pi/4$ (Bird's-eye view) (b) $\theta = \pi/4$ (Side view)

Fig. 8. Vorticity vector distributions above the scoured seabed at $\theta = \pi/4$.

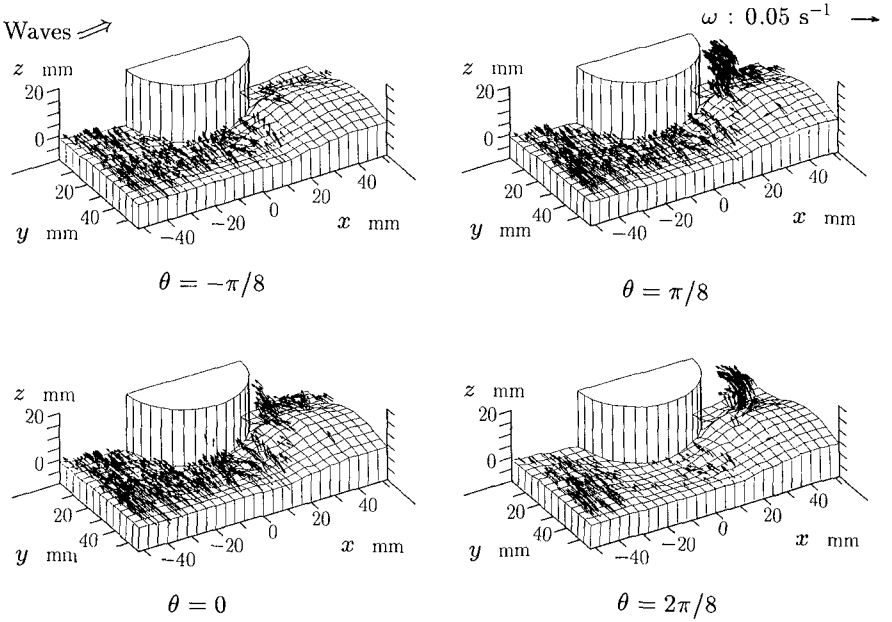

Fig. 9. Time evolution of the vortex above the scoured seabed.

arch-shaped one, as explained in the last section. Then this vortex drives local intense reversing flow close to the bed near the down-wave edge of the cylinder as shown in *Fig. 9.* Furthermore the flow produces the scour hole at the down-wave edge of the cylinder between two hills as represented in *Fig. 2.*

From the comparison between the vorticity distributions above the flat bottom and the scoured seabed, it is thus concluded that the deformation of the vortex shed from the cylinder is caused by the effect of the locally scoured seabed configuration. In other words, the rugged seabed topography causes change in the shedding and developing processes of the large vortex from the quasi-two-dimensional to the complex three-dimensional structure.

4. NUMERICAL SIMULATION

4. 1. Vortex-Segment-Model

A three-dimensional Vortex-Segment-Model has been adopted to simulate the flow around a cylinder. This model is one of the Discrete-Vortex-Methods, which deal with a flow field as a vorticity field and are useful to understand the behavior of vortices. Since an element of this model is a vortex segment with finite length, each segment does not satisfy Kelvin's circulation theorem rigidly. However, the model treats a vortex filament as a group of the segments, and hence the theorem is almost fulfilled in this model. Its validity has been reported by Shirayama *et al.* (1984) and others. Differing from the other Discrete-Vortex-Methods, this model can easily express the cut-and-connect processes of vortex filaments and the production of vorticity on the surfaces of solid boundaries due to the non-slip boundary condition. This model is thus useful to simulate the flow fields with the solid boundaries in them.

In this model the structure of a vortex segment is assumed as illustrated in *Fig. 10,* and an induced velocity vector for each vortex segment is given by

$$\boldsymbol{u}(\boldsymbol{x}) = -\frac{\Gamma}{4\pi}\int_{\boldsymbol{r}_1}^{\boldsymbol{r}_2} \frac{(\boldsymbol{x}-\boldsymbol{s})\times \boldsymbol{t}(\boldsymbol{s})}{|\boldsymbol{x}-\boldsymbol{s}|^3} d\boldsymbol{s}, \tag{7}$$

where $\boldsymbol{u}(\boldsymbol{x})$ is the induced velocity vector at a point $\boldsymbol{x}$, $\boldsymbol{s}$ is a position vector along the axis of the vortex segment, $\boldsymbol{t}(\boldsymbol{s})$ is a unit vorticity vector at the position $\boldsymbol{s}$, and $\boldsymbol{r}_1$ and $\boldsymbol{r}_2$ are the positions of the two ends of the segment. A finite core radius of the vortex segment is assumed in this model for the stability in numerical

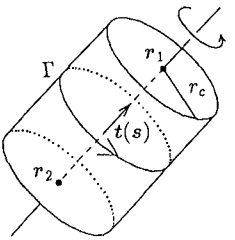

Fig. 10. The structure of a vortex segment in the Vortex-Segment-Model.

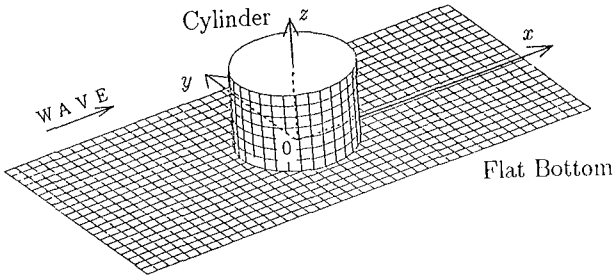

Fig. 11. Computational domain.

computation. To simulate the flow field, a large number of vortex segments are distributed in the computational domain.

4. 2. Results of the Simulation

The model has been applied to the numerical simulation of the near-bottom flow field around a vertical slender cylinder under waves. The bottom of the computational domain is flat as shown in *Fig. 11.* The non-slip condition is imposed on the surfaces both of the cylinder and of the flat bed, and therefore the vorticity is produced on these solid boundaries. The numerical simulation has been conducted under the condition that the Ursell number is 25 and the K.C. number is 5.0, which is close to that of the laboratory experiments.

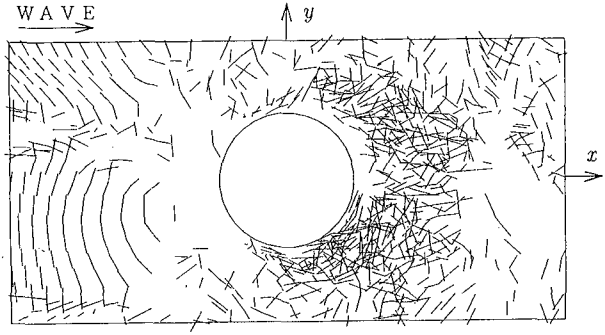

(a) Top View

(b) Side View

Fig. 12. Vortex segment distributions at $\theta = \pi/4$.

To satisfy the solid boundary conditions mirror-imaged vortex segments are introduced for the flat bottom boundary, and fixed vortex segments are put on the surface of the cylinder. In addition, new vortex segments are generated in close proximity from the solid boundaries to satisfy the non-slip condition in every computational steps.

Figure 12 displays one of the vortex segment distributions obtained by this model. As shown in this figure, flow fields are represented with a number of vortex segments. Under the computational conditions of this study, the distributions of vortex segments are almost symmetric with respect to the vertical x-z plane, which is consistent with the experimental results.

The evaluated velocity distribution in the horizontal plane near the bed and the corresponding experimental result are shown in *Fig. 13*. It is found that the vortex shedding is well simulated in this case. These figures indicate a fairly good agreement, which implies the validity of this numerical model.

5. CONCLUSION

The near-bed velocity distributions around the vertical slender cylinder under waves have been measured and estimated in full detail above both the flat bottom and the scoured seabed. The following characteristics of the flow have been

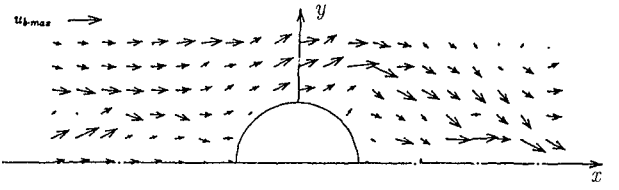

(a) Result of the Numerical Simulation ($z = D/20$)

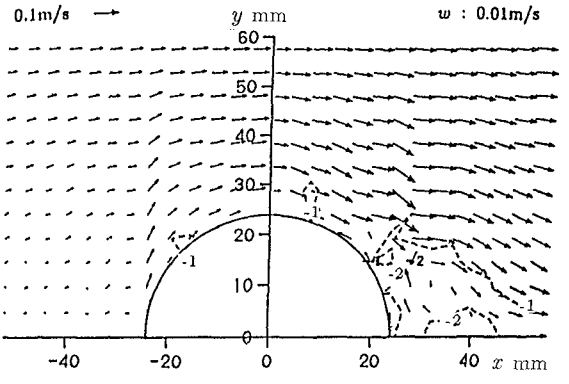

(b) Experimental Result ($z = D/8$)

Fig. 13. Velocity distribution in a horizontal plane at $\theta = \pi/4$.

found. Above the flat bottom, the axis of the vortex shed from the cylinder surface is almost straight and vertical. On the other hand, the arch-shaped vortex is formed over the scoured seabed. This arch-shaped vortex drives the local intense reversing flow close the bed near the down-wave edge of the cylinder. It is therefore clear that the rugged seabed shape has a significant influence on the shedding and deforming processes of large vortices to change the flow pattern from the quasi-two-dimensional to the complex three-dimensional structure. Since this three-dimensional vortices cause local intense flow near the bed, the behavior of the vortices is thus very important to study local scouring processes around a vertical cylinder.

In addition the flow around a cylinder over the flat bottom has been simulated numerically with a three-dimensional Vortex-Segment-Model. The results of the simulation have shown a good agreement with those obtained in the laboratory experiments. Hence it is concluded that the numerical model presented here is a promising one for analysis of the scour process and for prediction of the scouring.

ACKNOWLEDGEMENTS

I thank Professors A. Watanabe and M. Isobe of the University of Tokyo for their suggestions in this study.

REFERENCES

Breusers, H. N. C., G. Nicollet, and H. W. Shen (1977): Local scour around cylindrical piers, Journal of Hydraulic Research, Vol.15, No.3, pp.211–252.

Hino, M., Y. Meng and M. Murakami (1989): An attempt of estimating a whole instantaneous velocity field from sparse velocity data, Technical Report No.41, Dept. of Civil Eng., Tokyo Institute of Technology, pp.1–8. (in Japanese)

Nishizawa, M. and M. Sawamoto (1988): Local scour around a vertical cylinder under the wave action, Proc. of the 6th Congress of APD–IAHR, pp.121–128.

Sharman, C. A. (1978): A mass-consistent model for wind fields over complex terrain, Journal of Applied Meteorology, Vol.17, pp.312–319.

Shen, H. W., V. R. Schneider and S. Karaki (1969): Local scour around bridge piers, Journal of the Hydraulics Division, ASCE, Vol.95, HY6, pp.1919–1940.

Shirayama, S. and K. Kuwahara (1984): Vortex method in three-dimensional flow, Proc. of the 9th Inter. Conf. on Numerical Methods in Fluid Dynamics, Springer, pp.503–507.

Sumer, B. M., J. Fredsøe, and N. Christiansen (1992): Scour around vertical pile in waves, Journal of Waterways, Port, Coastal and Ocean Engineering, ASCE, Vol.118, No.1, pp.15–31.

Wells, D. R. and R. M. Sorensen (1970): Scour around a circular cylinder due to wave motion, Proc. of the 12th Coastal Eng. Conf., pp.1263–1279.

A description of the "acqua alta" event on 5th October

the Organizing Committee

Introduction

""Certainly the "acqua alta" on the first morning of the Conference was a memorable event which every coastal engineer should experience in part because it underscores one of the problems that may face the next generation of coastal engineers. Our colleagues that were unable to attend the Conference will be envious of the *opportunity* to wade to the first session, barefoot and shoes and socks in hand! The sessions and chapters in the Proceedings on the history and plans relating to Venice Lagoon and the protective barrier islands will serve as valuable source documents for the future. The venue in Venezia was both appropriate and unforgettable."" (from a letter of Robert Dean).

What a better introduction than these few words of the new CERC President. Following this stimulation the Organizing Committee has asked some near participants[1] to supply a description of the event in order to fix the experience of those who were present and to give a pale idea to those who could not attend the Conference.

The meteo- and oceanographic situation

On the first days of October 1992 the meteorological situation over the Mediterranean Sea was characterized by an almost uniform and relatively high atmospheric pressure distribution. Wind speeds and wave heights were very low throughout the basin, due mainly to local actions. This situation changed abruptly on October 3rd (Saturday), when an energetic flow of north-westerly cold air entered the Gulf of Lion from the Carcassonne passage between the Pyrenées and the Massif Central in south-western France (see figure 1.a, relative to 00 UTC 3 October '92).
Interacting with the still warm water of the Western Mediterranean Sea, this led to an intense cyclogenesis. A low centered over Corsica developed (see figure 1.b, relative to 00 UTC 4 October '92) with southerly winds on its eastern side, i.e. over Italy. The flow was intensified by the opposing high pressure zone located over eastern and northern Europe.

The southerly wind produced high wave conditions on the Ionian Sea, particularly on the facing Italian coasts. Over the Adriatic Sea the parallel Appennines ridge on the Italian side and the Dynaric Alps on Yugoslavia

[1]Luciana Bertotti, CNR-ISDGM Venice, provided the meteorological description, Manlio De Boni, TEI Milano, the wave records, Giovanni Cecconi, Consorzio Venezia Nuova, and Paolo Canestrelli, Centro Previsioni Maree Venezia, provided the description of the tide, Leopoldo Franco and Ferruccio Egori the photographs.

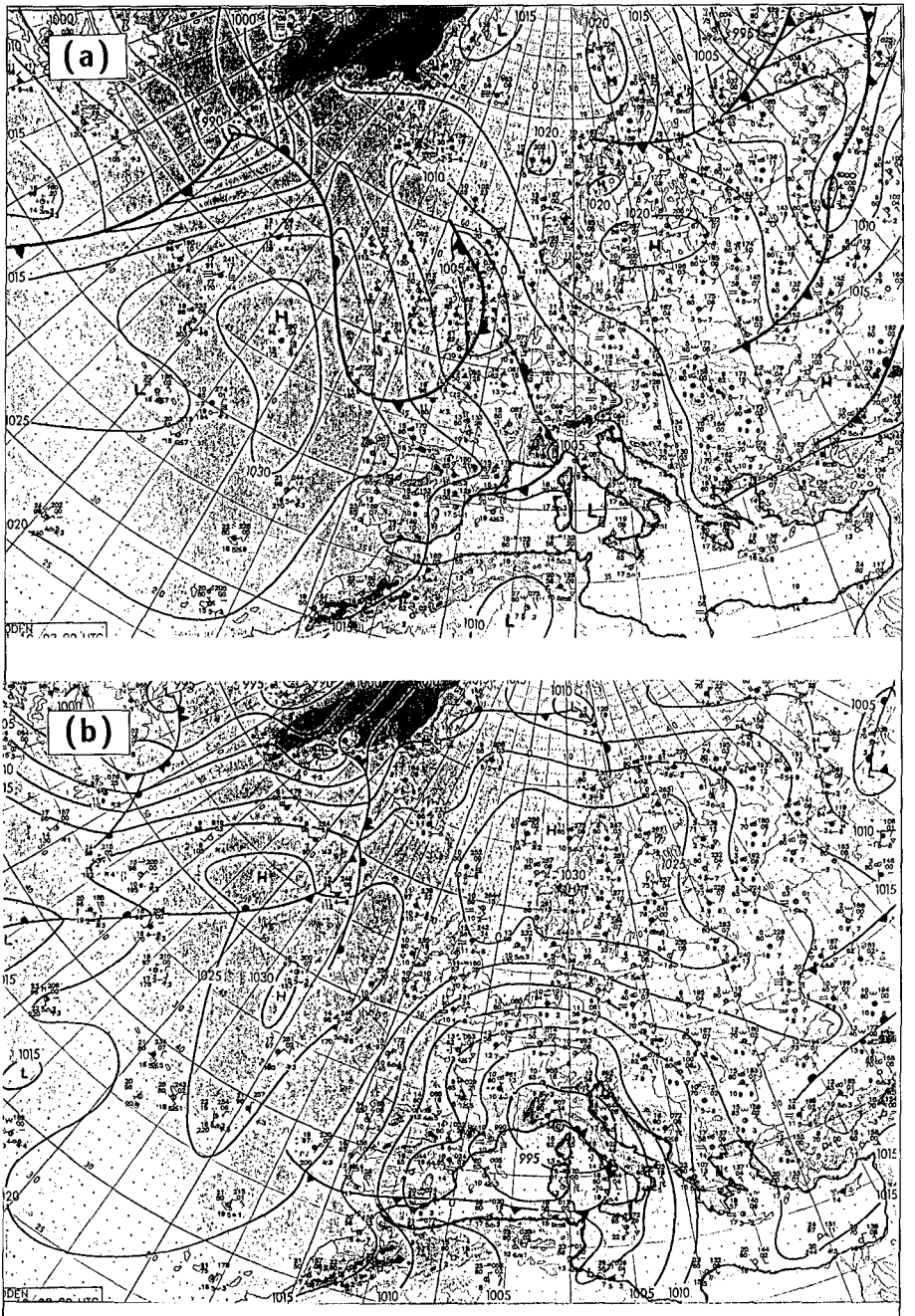

Fig. 1. Weather map at 3-10-92 (a) and 4-10-92 00 UTC (b)

channeled the flow leading to an intense south-easterly wind all along the Adriatic Sea. This is well shown by the distribution of surface wind at 06 UTC 4 October '92 obtained with the meteorological model of the European Center for Medium Range Weather Forecasts, Reading, U.K. (see figure 2).

Wave reacted rapidly. The peak conditions were reached in the first 12 hours of 4 October, with significant wave height $H_s = 2.0$ m at Pescara, in the mid Adriatic, and $H_s = 3.4$ m at the oceanic platform of ISDGM, 8 miles off the coast of Venice. The two positions, together with the more southerly Monopoli location in the Adriatic Sea and Crotone in the Ionian coast, are indicated by black dots in figure 2. Figure 3 shows the time series of H_s at these four locations throughout the storm.

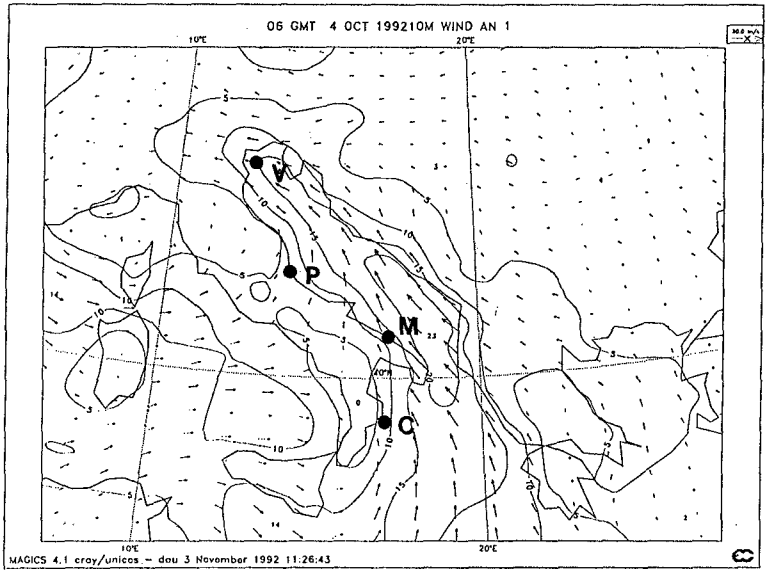

Fig. 2. Surface wind on 4-10-92 06 GMT and wave gauge locations

The later decrease of wind speed, following the expansion and filling of the atmospheric low, left in the Adriatic Sea a swell propagating towards North-West, clearly recognizable in the records of figure 3.

The storm surge in Venice

On Sunday the 4th, at neap tide, without any storm surge, a maximum level of 40 cm due only to the astronomical tide was expected at Punta della Salute, but because of the strong wind along the Adriatic Sea and the local atmospheric low pressure the water level reached 119 cm, with a storm surge component of about 80 cm (see figure 4).

Due to the persistent meteorological conditions, the water level raised on

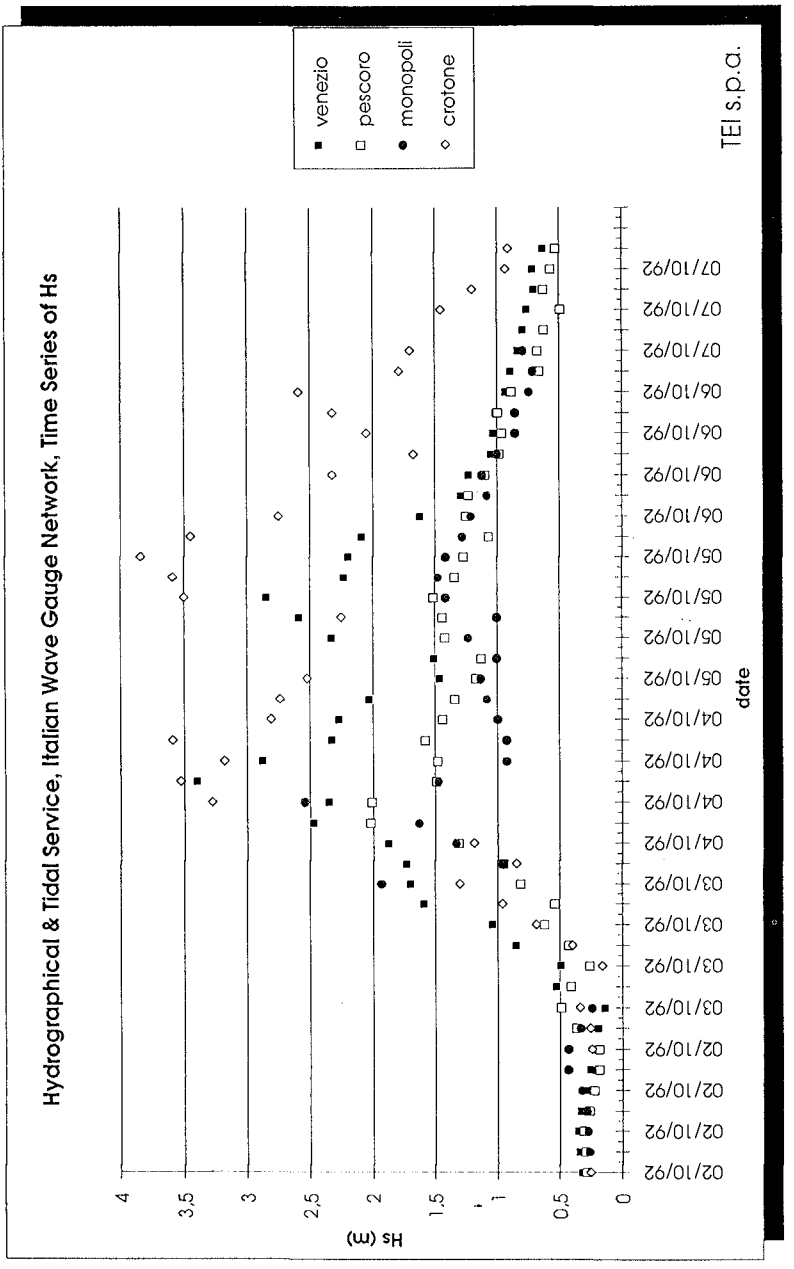

Fig. 3. Time history of recorded wave height in the Adriatic Sea

the following day, the first day of the Conference, flooding the town since 6 am. The flood lasted almost five hours till 11 am reaching the maximum level of 126 cm at 9 am just in time for the opening lecture. During the peak San Marco Square was covered by 46 cm of water and 50 % ot the town was flooded.

Should the storm surge have occurred in a spring tide period, when the normal high water level is 75 cm, the water would have been 35 cm higher and the flood would have reached 80% of the town (cf. figure 5).

The effects

The flood caused more damages and delays than usual due to the peculiar time of occurrence: early on Monday morning, following immediately a holiday. Visitors in particular had difficulties in getting a pair of boots and the 120 cm high walk-ways were not high enough to give a dry passage to the people without boots.

Photo 1 gives you a "look of the quay" near San Marco Square on Monday morning. On the opposite side of the channel participants in the Conference were entering Fondazione Cini with some trouble, cf. photo 2.

Notwithstanding the surprise of participants in the Conference, the flood on Monday October the 5th was not an exceptional one. During the years 1980-'89 this level was exceeded twelve times (cf. figure 5) and its return period is close to one year.
Comparing this flood to historical records, the water depth reached in San Marco Square was just one third of that reached on November 4th 1966, when the most severe recorded flood reached 114 cm water depth in San Marco Square (194 cm recorded water level).
The Conference event was actually much more unexpected than his bare return period tells. Actually most events occurs in late fall and winter and near spring tide and the return period of the "unexpected" storm surge is about 5 years. The sturm surge may be decomposed into a quasi static component and in a seiche component, whose main period is ~ 21 hr. During sunday and monday the seiche component was in phase with the astronomical tide; in the following days the seiche amplitude was decreasing and the phase was lost, determining a rapid reduction of high water level.

Subsidence has some influence on the effects of high storm surge events. The reference level above which tide is measured in Venice is the mean sea level in 1897. Nowaday the mean sea level as a consequence mainly of subsidence is about 22 cm above datum and increases at the approximate rate of 0.1 cm/year.

Table 1. Components of tide elevation in Venice, [cm]

	Normal spring tide	4 Nov. '66	5 Oct. '92	Normal "acqua alta"
Mean sea level	22	20	22	22
Astronomical tide	50	25	20	38
Storm surge	–	150	84	60
quasi static	–	100	40	30
seiche	–	50	44	30

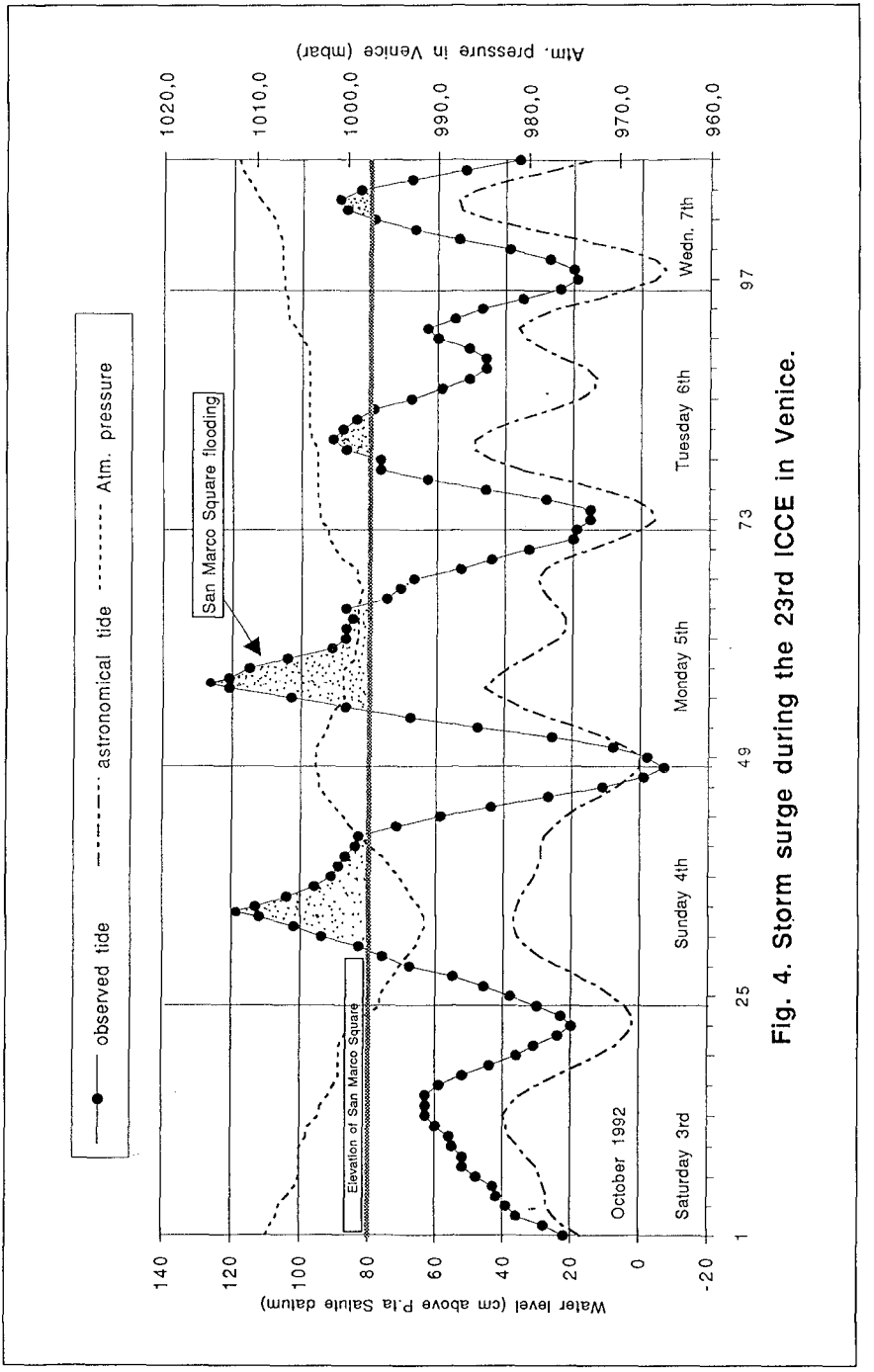

Fig. 4. Storm surge during the 23rd ICCE in Venice.

Photo 1. San Giorgio Island from San Marco Square on Monday morning

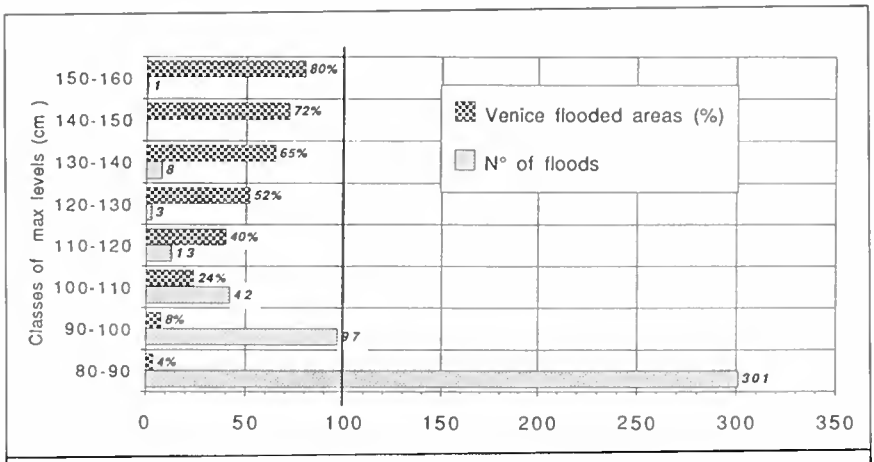

Fig. 5. Number of floods in Venice in the ten years from 1980 to '89

Photo 2. Delegates entering Fondazione Cini on Monday morning